

Correct structural index in Euler deconvolution via base-level estimates

Felipe F. Melo¹ and Valéria C. F. Barbosa¹

ABSTRACT

In most applications, the Euler deconvolution aims to define the nature (type) of the geologic source (i.e., the structural index [SI]) and its depth position. However, Euler deconvolution also estimates the horizontal positions of the sources and the base level of the magnetic anomaly. To determine the correct SI, most authors take advantage of the clustering of depth estimates. We have analyzed Euler's equation to indicate that random variables contaminating the magnetic observations and its gradients affect the base-level estimates if, and only if, the SI is not assumed correctly. Grounded on this theoretical analysis and assuming a set of tentative SIs, we have developed a new criterion for determining the correct SI by means of the minimum standard deviation of base-level estimates. We performed synthetic tests simulating multiple magnetic sources with different SIs. To produce mid and strongly interfering synthetic magnetic anomalies, we added constant and

nonlinear backgrounds to the anomalies and approximated the simulated sources laterally. If the magnetic anomalies are weakly interfering, the minima standard deviations either of the depth or base-level estimates can be used to determine the correct SI. However, if the magnetic anomalies are strongly interfering, only the minimum standard deviation of the base-level estimates can determine the SI correctly. These tests also show that Euler deconvolution does not require that the magnetic data be corrected for the regional fields (e.g., International Geomagnetic Reference Field [IGRF]). Tests on real data from part of the Goiás Alkaline Province, Brazil, confirm the potential of the minimum standard deviation of base-level estimates in determining the SIs of the sources by applying Euler deconvolution either to total-field measurements or to total-field anomaly (corrected for IGRF). Our result suggests three plug intrusions giving rise to the Diorama anomaly and dipole-like sources yielding Arenópolis and Montes Claros de Goiás anomalies.

INTRODUCTION

Euler deconvolution is one of the most popular techniques in potential field methods. It is a semiautomatic interpretation technique proposed by [Reid et al. \(1990\)](#), which allows fast processing of large data sets. The technique is grounded on Euler equation for homogeneous functions ([Hood, 1965](#); [Thompson, 1982](#)). Euler deconvolution relates potential-field measurements, their gradients, and a given integer number called the structural index (SI), which in turn depends on the nature (type) of the geologic source ([Henderson and Zietz, 1948](#); [Smellie, 1956](#); [Stavrev and Reid, 2007](#); [Reid and Thurston, 2014](#); [Uieda et al., 2014](#)). Usually, Euler deconvolution assumes a tentative SI and estimates four parameters, such as base level, horizontal and vertical positions of an isolated, and single-point geologic source.

One practical hindrance for Euler deconvolution is the need to assume a tentative SI. The SI can only be an integer number

([Mas-Colell et al., 1995](#); [Ravat, 1996](#); [Thurston, 2010](#); [Reid and Thurston, 2014](#); [Reid et al., 2014](#)); otherwise, the index changes under the variation of the source-observation vector ([Ravat, 1996](#); [Reid and Thurston, 2014](#)). Assuming some tentative SI values, [Thompson \(1982\)](#) notices the relation between the use of the correct SI and a tight clustering in depth estimates and uses this behavior to determine the correct SI. Other authors, such as [Reid et al. \(1990\)](#), follow this approach to propose slight modifications of [Thompson's \(1982\)](#) criterion for determining the SI. Following this approach, other authors propose other techniques (e.g., [Mikhailov et al., 2003](#); [Ugalde and Morris, 2010](#)) to treat the spreading of depth solutions and define the correct SI. [Silva et al. \(2001\)](#) show that the criterion for determining the SI as the tentative value producing the smallest solution scattering, that includes the depth estimates, is theoretically sound but can fail in practice because of data noise. On the other hand, [Barbosa et al. \(1999\)](#) show that the minimum

Manuscript received by the Editor 27 November 2017; revised manuscript received 8 June 2018; published ahead of production 26 July 2018; published online 09 October 2018.

¹Observatório Nacional, Rio de Janeiro, Brazil. E-mail: felipe146@hotmail.com; valcris@on.br

© 2018 Society of Exploration Geophysicists. All rights reserved.

correlation between base-level estimates and profile magnetic data in modulus gives the correct SI, and Melo et al. (2013) use this approach in gridded magnetic data. Alternatively, some authors modified Euler deconvolution and develop new techniques solving for SI and depth simultaneously (Stavrev, 1997; Mushayandebvu et al., 2001; Nabighian and Hansen, 2001; Hsu, 2002; Keating and Pilkington, 2004; Fedi et al., 2009) or deal with nonideal sources (Stavrev and Reid, 2007, 2010; Thurston, 2010; Florio and Fedi, 2014; Fedi et al., 2015).

According to Thompson (1982), it is hard to detect the anomalous field by itself so he introduces the concept of base level that is a constant background value of the field inside an evaluating data window. He stresses that the base level can be generated, for example, by interfering anomalies or regional field. By handling the Euler deconvolution mathematically, some authors assumed a constant and nonnull base level (e.g., Thompson, 1982; Reid et al., 1990; Barbosa et al., 1999; Hsu, 2002), a null base level (Silva and Barbosa, 2003), linear base levels (e.g., Stavrev, 1997; Gerovska and Araúzo-Bravo, 2003), and nonlinear base levels (e.g., Pasteka, 2006; Dewangan et al., 2007). Although the base level is estimated by the Euler deconvolution, few authors have used this estimate in practice. Fairhead et al. (1994), for example, estimate and remove the base level from the anomaly to estimate focused Euler solutions in a two-step approach. Reid and Thurston (2014) state that it is possible to determine the correct SI using the base-level estimates; however, these estimates were only used by Barbosa et al. (1999) and Melo et al. (2013) to this end in a straightforward way.

In this paper, we show that realizations of random variables contaminating the potential-field measurements affect the base-level estimates if, and only if, the SI is not assumed correctly. Hence, we propose a criterion to determine the SI based on the standard deviation of the estimates of base level using different values of SI. The optimal SI is one that produces the smallest standard deviation of the base-level estimates. In our tests, we noticed that even for strongly interfering anomalies, the minimum standard deviation of base-level estimates gives the correct SI; however, it fails if the anomaly is not produced by a single-point source. We also confirmed that anomalies generate nonlinear base-level estimates even when the true simulated base level added to the data is constant or null (not shown). This happens not only because of the interfering anomalies but also because base-level estimates have a nonlinear pattern that mimics the potential-field anomalies even inside the current moving data window. Here, we show that anomaly interference produced by the presence of nonlinear background and nearby anomalies makes the criterion for determining the correct SI based on the smallest scattering of depth estimates unfeasible. Conversely, we certify the good performance of our approach in determining the correct SI by assuming null (not shown), constant, and nonlinear backgrounds that were added to the data. We applied our methodology to total-field measurements and total-field anomaly (corrected for International Geomagnetic Reference Field [IGRF]) from a portion of Goiás Alkaline Province (GAP) located in central Brazil, and the numerical results are similar. Both applications determine the same SI and mean depths for the geologic sources in the study area. These results show that the prior remove of the IGRF is not mandatory in Euler deconvolution application. The estimated base level reveals a nonlinear pattern that mimics the pattern of the anomaly. The Diorama anomaly is the main target alkaline intrusion to be interpreted in the study area. Our result suggests that Diorama

anomaly is generated by more than one plug intrusion. We also expanded our interpretation using Euler deconvolution to other anomalies in the study area (e.g., Arenópolis, Montes Claros de Goiás, and Córrego dos Bois). However, some of the results may not be reliable because the magnetic sources may not behave as single-point sources violating the concept of Euler homogeneity.

METHODOLOGY

Euler deconvolution is defined by Reid et al. (1990) as

$$(x - x_o) \frac{\partial h}{\partial x} + (y - y_o) \frac{\partial h}{\partial y} + (z - z_o) \frac{\partial h}{\partial z} = \eta(b - h), \quad (1)$$

where η is the SI, b is a base level or background value, x_o , y_o , and z_o are the source positions, x , y , and z are the observation positions, $h = h(x, y, z)$ is the total-field anomaly, and $\partial h / \partial x$, $\partial h / \partial y$, and $\partial h / \partial z$ are the gradients of anomaly with respect to the variables x , y , and z , respectively. We use a tentative SI in equation 1, in a moving data-window scheme, and the estimated parameters are \hat{x}_o and \hat{y}_o (horizontal positions of the source), \hat{z}_o (vertical position of the source), and \hat{b} (base level). The caret (hat) denotes an estimated quantity.

Here, we extend and modify the criterion of Barbosa et al. (1999) for determining the best SI for gridded data. By applying Euler deconvolution with a moving data-window scheme and the correct SI, η , over a region that encompass the anomaly, we obtain the estimated parameters \hat{x}_o^k , \hat{y}_o^k , \hat{z}_o^k , and \hat{b}^k for the k th position of the moving data window. Hence, equation 1 can be written as

$$\begin{aligned} & \hat{x}_o^k \frac{\partial h_i^k}{\partial x} + \hat{y}_o^k \frac{\partial h_i^k}{\partial y} + \hat{z}_o^k \frac{\partial h_i^k}{\partial z} + \eta \hat{b}^k \\ &= x_i^k \frac{\partial h_i^k}{\partial x} + y_i^k \frac{\partial h_i^k}{\partial y} + z_i^k \frac{\partial h_i^k}{\partial z} + \eta h_i^k, \end{aligned} \quad (2)$$

where the subscript i is related to the i th observation position (x_i , y_i , and z_i) inside the k th moving data window.

By assuming a wrong SI, μ , we obtain the estimates \hat{x}_o^k , \hat{y}_o^k , \hat{z}_o^k , and \hat{b}^k , and equation 1 can be rewritten as

$$\begin{aligned} & \hat{x}_o^k \frac{\partial h_i^k}{\partial x} + \hat{y}_o^k \frac{\partial h_i^k}{\partial y} + \hat{z}_o^k \frac{\partial h_i^k}{\partial z} + \mu \hat{b}^k \\ &= x_i^k \frac{\partial h_i^k}{\partial x} + y_i^k \frac{\partial h_i^k}{\partial y} + z_i^k \frac{\partial h_i^k}{\partial z} + \mu h_i^k. \end{aligned} \quad (3)$$

By subtracting equation 3 from equation 2 and rearranging the terms, we obtain

$$\begin{aligned} & (\hat{x}_o^k - \hat{x}_o^k) \frac{\partial h_i^k}{\partial x} + (\hat{y}_o^k - \hat{y}_o^k) \frac{\partial h_i^k}{\partial y} + (\hat{z}_o^k - \hat{z}_o^k) \frac{\partial h_i^k}{\partial z} \\ &+ \mu \hat{b}^k - \eta \hat{b}^k = (\mu - \eta) h_i^k. \end{aligned} \quad (4)$$

Let us assume that additive random noises ε_1 , ε_2 , ε_3 , and ε_4 contaminate, respectively, the terms $\partial h_i^k / \partial x$, $\partial h_i^k / \partial y$, $\partial h_i^k / \partial z$, and h_i^k . Accordingly, equation 4 can be rewritten as

$$\begin{aligned} & (\hat{x}_o^k - \hat{x}_o^k) \left[\frac{\partial h_i^k}{\partial x} + \varepsilon_1 \right] + (\hat{y}_o^k - \hat{y}_o^k) \left[\frac{\partial h_i^k}{\partial y} + \varepsilon_2 \right] + (\hat{z}_o^k - \hat{z}_o^k) \\ & \times \left[\frac{\partial h_i^k}{\partial z} + \varepsilon_3 \right] + \mu \hat{b}^k - \eta \hat{b}^k = (\mu - \eta) [h_i^k + \varepsilon_4]. \end{aligned} \quad (5)$$

As shown by Silva and Barbosa (2003), the estimates of the horizontal source positions are not affected by the choice of the SI because these estimates do not depend on the SI. Hence, even assuming a wrong SI, μ , we have that $\hat{x}_o^k = \hat{x}_o^k$ and $\hat{y}_o^k = \hat{y}_o^k$. As result, the first and second terms on the left side of equation 5 are very close to zero. Thus, rearranging equation 5, we have

$$\hat{b}^k = \frac{\eta \hat{b}^k}{\mu} + \frac{(\hat{z}_o^k - \hat{z}_o^k)}{\mu} \left[\frac{\partial h_i^k}{\partial z} + \varepsilon_3 \right] + \left(1 - \frac{\eta}{\mu} \right) [h_i^k + \varepsilon_4]. \quad (6)$$

Notice that the second and third terms on the right side of equation 6 are corrupted with random variables (ε_3 and ε_4). Hence, estimates of the base level can be affected by uncertainties in the total-field data h_i^k and in its vertical gradient $\partial h_i^k / \partial z$. However, random variables do not affect base-level estimates if, and only if, we assume the correct SI (i.e., if $\mu = \eta$). Only in this case, we have $\hat{z}_o^k = \hat{z}_o^k$ and the second and third terms on the right side of equation 6 are negligible. Therefore, equation 6 shows that the presence of random noise will affect the base-level estimates if we do not correctly assume the SI (i.e., if $\mu \neq \eta$). In this case, the terms $(\hat{z}_o^k - \hat{z}_o^k) / \mu [(\partial h_i^k / \partial z) + \varepsilon_3]$ and $(1 - (\eta / \mu)) [h_i^k + \varepsilon_4]$ in equation 6 will be nonnegligible.

Let us assume a set of L moving data windows and thus, a set of L base-level estimates using either a wrong SI ($\hat{b}^1, \dots, \hat{b}^L$) or the correct SI ($\hat{b}^1, \dots, \hat{b}^L$). Thus, the standard deviation of base-level estimates obtained over the anomaly will be minimum only if the SI is correctly assumed (i.e., $\mu = \eta$).

In our approach, we provisionally assigned a tentative SI. For each SI, we estimate four parameters \hat{x}_o , \hat{y}_o , \hat{z}_o , and \hat{b} , which are plotted against the central position of the moving data window forming maps as proposed by Silva and Barbosa (2003). The maps of \hat{x}_o and \hat{y}_o form plateaus over the anomaly (Silva and Barbosa, 2003; Melo et al., 2013); however, plateaus may not be clearly formed for depth (\hat{z}_o) and base-level (\hat{b}) estimates in the presence of interfering anomalies. By assuming any tentative SI, we propose to evaluate the standard deviation of base-level estimates over an area delineated by depth estimates that lie over the anomaly. In the presence of interfering anomalies, we delineate this area using the approach of Melo et al. (2013), which is defined through the intersection of mapped plateaus on horizontal estimates (\hat{x}_o and \hat{y}_o). The minimum standard deviation of a set of estimated base levels will define the correct SI. With the knowledge of the correct SI, the average of depth estimates in the area previously selected can give one solution per anomaly (Melo et al., 2013).

SYNTHETIC TESTS

We applied our methodology to different geologic scenarios in which the magnetic sources are approximated by simple geometry (Hinze et al., 2013). However, these simple geometries represent real geologic bodies such as a semi-infinite prism simulating a fault

(SI = 0), a line of poles simulating a vertical sheet or thin dike (SI = 1), a point pole simulating a vertical cylinder or a plug/pipe (SI = 2), and a dipole simulating a sphere or a magmatic chamber/unexploded ordnance (UXO) (SI = 3).

In the first test, we assume a constant background value, simulating the magnetic field on a region. In the second test, we simulate a nonlinear background; this background can be generated by a strong magnetic source or poor definition of the IGRF. Finally, in the last test, we simulate constant and nonlinear backgrounds and approximate the sources distance, generating strong-interfering anomalies more close to real-world scenario.

In all tests, we run Euler deconvolution using tentative SIs of 0, 1, 2, and 3. The moving data window size is 9×9 grid points, following the recommendation of Reid et al. (2014) about window size, grid space, and depth of investigation. Throughout these tests, values of declination, inclination, and total-field intensity were based on Chulliat et al. (2014), simulating the field in Phoenix, Arizona, USA, and derivatives were calculated in the Fourier domain (Blakely, 1996). All anomalies were corrupted with pseudorandom Gaussian noise with zero mean and standard deviation of 0.01 nT. We assume a coordinate system with the x -axis increasing north, y -axis increasing east, and z -axis increasing down. The surveys were simulated on plane $z = 0$ km at a grid of 325×300 observation points in the north and east directions, with a regular equal space of 0.2 km in the north and east directions.

Test 1 — Constant background

Figure 1 shows the synthetic noise-corrupted total field anomaly produced by semi-infinite prism (SI = 0), a line of 1220 poles (SI = 1) separated by grid distance, a monopole (SI = 2), and a sphere (SI = 3) of radius 0.5 km. The simulated geomagnetic field has an inclination of 59° and a declination of 10° with a constant

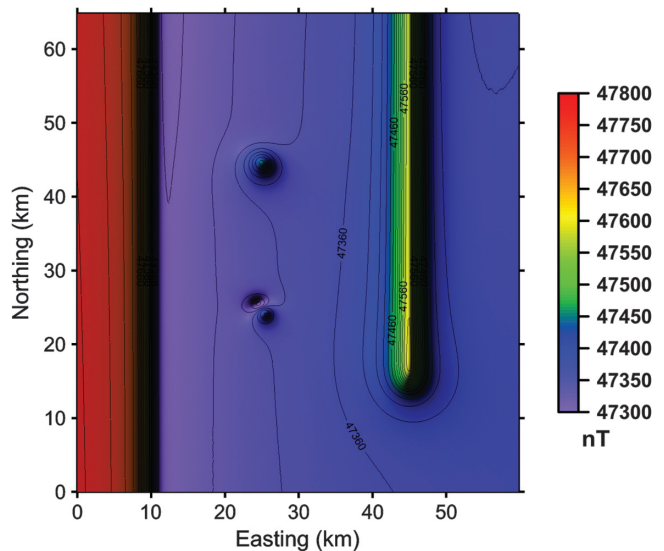


Figure 1. Noise-corrupted total-field anomaly generated by a prism (SI = 0), a line of poles (SI = 1), a single pole (SI = 2), and a dipole (SI = 3). The simulated geomagnetic field with intensity of 47,500 nT has an inclination of 59° and a declination of 10° . The dipole is magnetized uniformly, with magnetization intensity of 5 A/m, magnetization inclination of 9° , and declination of -32° , whereas the other sources are magnetized by induction only.

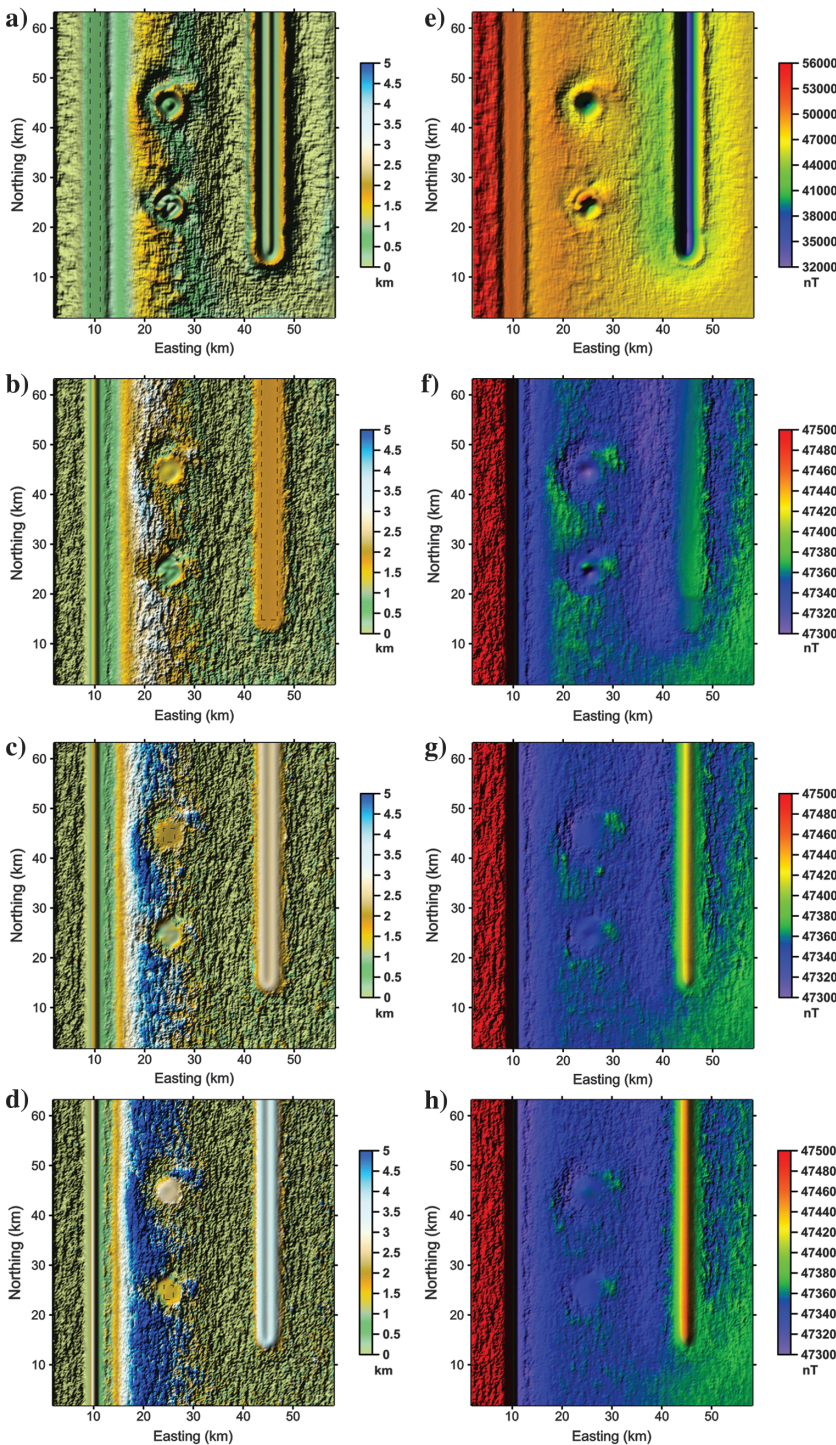


Figure 2. Euler deconvolution estimates for anomaly with constant background (Figure 1). (a-d) Depth and (e-h) base-level estimates assuming SIs of 0, 1, 2, and 3, respectively. Depth estimates assuming the correct SI form a plateau of correct values, whereas estimates using the wrong SI not only failed to form a plateau but they also failed in their estimates. Base-level estimates using the correct SI has minimum values compared with the estimates using the wrong SI. For each source, the plateau areas, where the methodology is applied, are outlined by the dashed rectangles. These areas were defined by the plateaus on the depth estimates shown in (a-d).

intensity of 47,500 nT. The prism with magnetization intensity of 1 A/m extends infinitely along the x -direction, from 10 km to the infinite along the y -direction, and in depth from 0.5 km to infinite. The line of poles is located at $y_o = 45$ km and $z_o = 1.8$ km and extends from $x_o = 15$ to infinite, each pole has magnetization intensity of 0.5 A/m. The single pole is located at $x_o = 45$ km, $y_o = 25$ km, and $z_o = 2$ km, with magnetization intensity of 5 A/m. Finally, the sphere is magnetized uniformly, with magnetization intensity of 5 A/m, magnetization inclination of 9°, and declination of -32°. The sphere is located at $x_o = 25$ km, $y_o = 25$ km, and $z_o = 1.5$ km. Although applied to a constant base level, the results shown in this test were also applied to a null base level (not shown), i.e., magnetic anomaly corrected for IGRF. By inspecting Figure 1 qualitatively, we can note a subtle distortion of the data isovalue curves that indicate weakly interfering anomalies due to the proximity between the simulated sources.

Figure 2a–2d shows the depth estimates from Euler deconvolution assuming SIs of 0, 1, 2, and 3, respectively. For depth estimates, plateaus of solutions appear only when the correct SI is used, for non- or weak-interfering anomalies. When the wrong SI is used, depth estimates do not define a plateau; rather, they form a cavity or a prominence. A plateau of depth estimates is clearly evident in Figure 2a over the edge of the prism because the correct SI = 0 is used; whereas in Figure 2b–2d, we can see protuberances for the depth estimates of this source. The same occurs for the line of poles, single pole, and dipole, with respect to their correct SIs. Table 1 shows standard deviations of depth estimates using four different SI values for each source and considering this test with a constant background. The minimum standard deviation for each source (highlighted in boldface) occurs if the correct SI is used.

Figure 2e–2h shows the base-level estimates from Euler deconvolution assuming SIs of 0, 1, 2, and 3. These estimates fall at the same positions as depth estimates (Figure 2a–2d) and exhibit the same pattern when the correct SI is used. Specifically, a plateau of constant base-level estimates is exhibited when the correct SI is used, whereas cavities or bulges appear when the wrong SI is used. Thus, comparing at the same source position using different SI is easy to identify that the smallest variation of the base-level estimates at source location indicates the correct SI. In addition, notice that the base-level estimates mimic the magnetic anomaly (Figure 1). Later in this paper, this nonlinear pattern of the base-level estimates will show up clearly. Table 2 shows standard deviations of base-level estimates using four different SI values for each simulated source. The mini-

mum standard deviation for each source is in boldface. As expected, for each source, the standard deviation is minimum using the correct SI. Once the correct SI is defined, the mean depth calculated in the same area gives the correct depth of the sources.

The areas used to calculate the standard deviations of depth (Table 1) and base-level (Table 2) estimates are outlined in Figure 2a–2d (the dashed rectangles) for each source. These areas were defined by the plateau areas in the depth estimates.

This test shows that the minima standard deviations calculated either from base-level estimates (Table 2) or from depth estimates (Table 1) are able to correctly define SI in the presence of a constant background. In addition, this test shows that a constant background does not interfere in Euler deconvolution estimates. Therefore, the magnetic data do not need to be previously corrected for IGRF to the application of Euler deconvolution.

Test 2 — Nonlinear background

Here, we generated a synthetic total-field anomaly (Figure 3a) produced by the same sources and magnetization direction of the previous test. In this test, a simulated nonlinear background (Figure 3b) is added to the original data (Figure 3a) by

$$b(x_i, y_i) = \frac{(x_i + 10)(y_i + 10)}{30}, \quad (7)$$

giving rise to the noise-corrupted magnetic anomaly (Figure 3c) to be used in Euler deconvolution. In equation 7, the subscript i is related to the i th observation position (x_i, y_i) . This polynomial can simulate a regional field, a strongly interfering anomaly, or a poor definition of the IGRF. Notice that the nonlinear background (Figure 3b) has high values of the same order of magnitude as

Table 1. Standard deviations of depth estimates for the constant background.

Source	SI = 0	SI = 1	SI = 2	SI = 3
Prism	0.002	0.277	0.555	0.833
Line of poles	0.109	0.017	0.113	0.222
Pole	0.095	0.057	0.051	0.086
Dipole	0.102	0.068	0.041	0.037

Minimum standard deviation for each source is highlighted in boldface.

Table 2. Standard deviations of base-level estimates for the constant background.

Source	SI = 0	SI = 1	SI = 2	SI = 3
Prism	86.436	124.742	124.949	125.040
Line of poles	2959.662	4.451	15.550	20.226
Pole	1869.891	9.835	2.989	4.169
Dipole	3244.212	21.072	5.074	1.970

Minimum standard deviation for each source is highlighted in boldface.

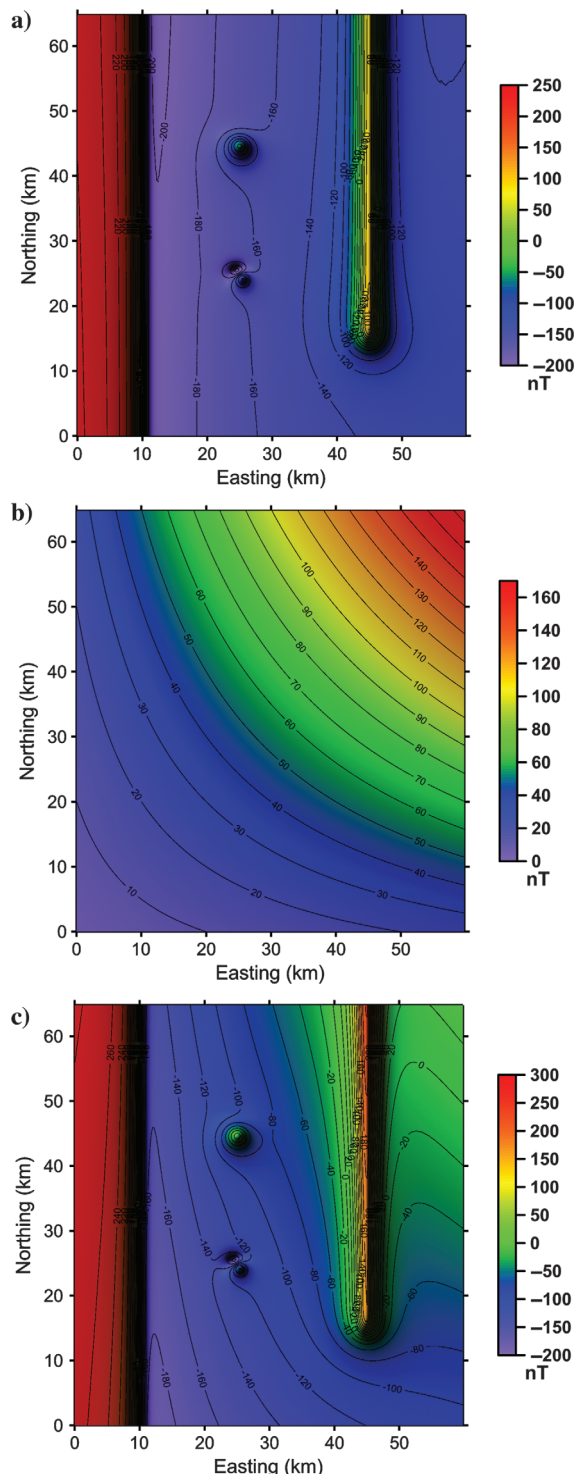


Figure 3. Nonlinear background anomaly. (a) Noise-corrupted total-field anomaly generated by a prism (SI = 0), a line of poles (SI = 1), a single pole (SI = 2), and a dipole (SI = 3). The simulated geomagnetic field with intensity of 47,500 nT has inclination of 59° and declination of 10°. The dipole is magnetized uniformly, with magnetization intensity of 5 A/m, magnetization inclination of 9°, and declination of -32°, whereas the other sources are magnetized by induction only. (b) Nonlinear polynomial to simulate a regional field. (c) Noise-corrupted magnetic anomaly obtained by adding the total-field anomaly shown in (a) to the nonlinear polynomial shown in (b).

the original data (Figure 3a) producing strongly interfering anomalies, as displayed in Figure 3c.

In Figure 4a–4d, we can see depth estimates from Euler deconvolution assuming SIs of 0, 1, 2, and 3, respectively. Figure 4b

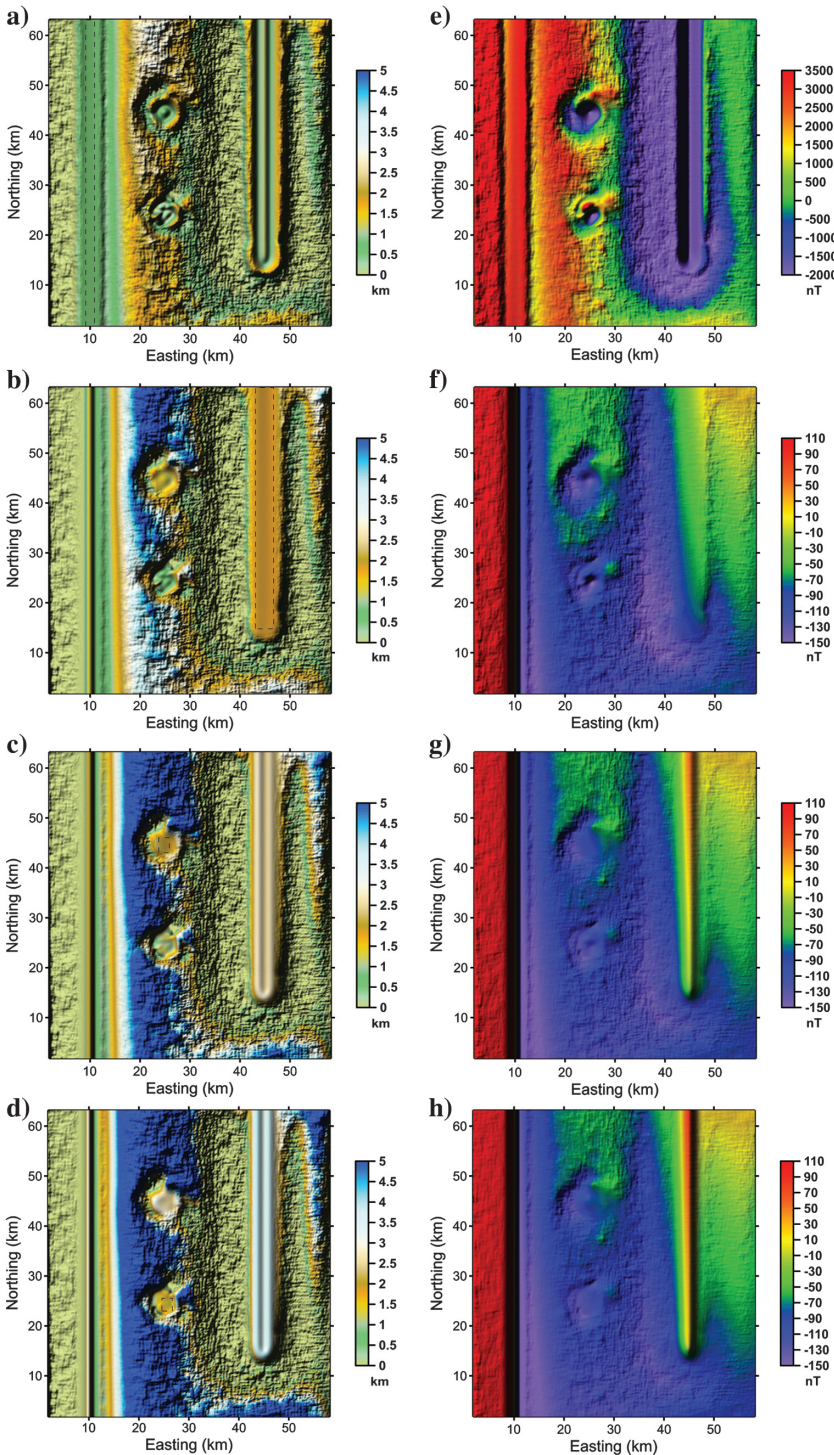


Figure 4. Euler deconvolution estimates for anomaly with nonlinear background (Figure 3c). (a-d) Depth and (e-h) base-level estimates assuming SIs of 0, 1, 2, and 3, respectively. For each source, the plateau areas, where the methodology is applied, are outlined by the dashed rectangles. These areas were defined by the intersection of mapped plateaus on horizontal estimates (\hat{x}_o and \hat{y}_o) shown in Figure 5.

shows the plateau on the depth estimates over the line of poles with a too-light difference compared with Figure 2b. In contrast, by comparing Figure 4c and 4d with Figure 2c and 2d, we notice that depth estimates of the correct sources for SIs 2 and 3 do not form

plateaus and show different shapes. This means that the depth estimates are affected by the presence of a nonlinear background. In a case like this, where the plateaus are not clearly defined on depth estimates (Figure 4c and 4d), we use the procedure of Melo et al. (2013), which delineates the plateau areas, to determine in our work the best SI, through the intersections of the plateaus formed on the horizontal estimates (\hat{x}_o and \hat{y}_o). Figure 5 shows the horizontal estimates using Euler deconvolution applied to noise-corrupted magnetic anomaly (Figure 3c) in the presence of nonlinear background. Figure 5a–5d shows the \hat{x}_o estimates, and Figure 5e–5h shows the \hat{y}_o estimates assuming SIs of 0, 1, 2, and 3, respectively. Because these horizontal estimates (\hat{x}_o and \hat{y}_o) are less sensitive to interfering anomalies than \hat{z}_o estimates, the intersections of the plateaus of \hat{x}_o (Figure 5a–5d) and \hat{y}_o (Figure 5e–5h) are used in this test to delineate the areas (shown in the dashed rectangles in Figure 4a–4d), which are used to determine the best SI.

Table 3 shows the standard deviations for depth estimates in the presence of a nonlinear background, and the minimum standard deviation for each source is in boldface. For the prism and the line of poles, the minima standard deviations of depth estimates indicate the correct sources. However, in contrast with the previous test, the minimum standard deviation for the pole indicates SI = 1 and for the dipole indicates SI = 2, which are the wrong SIs for these sources. Let us recall that the correct SI to a pole-like source is SI = 2 and a dipole-like source is SI = 3. Thus, the presence of a nonlinear background gives rise to some interference in depth estimates.

Figure 4e–4h shows the base-level estimates from Euler deconvolution assuming SIs of 0, 1, 2, and 3, respectively. The presence of a nonlinear background yields interfering anomalies (Figure 3c) that lead to strongly deformed base-level estimates (Figure 4e–4h). Thus, this presence makes it much harder to “see” the plateaus in Figure 4e–4h that were clearly viewed in the previous test with a constant background (Figure 2e–2h). Table 4 shows the standard deviations of base-level estimates for the nonlinear background test. The minima standard deviations of base-level estimates, in boldface, confirm the correct SI of each source.

This test shows that the minimum standard deviation of base-level estimates (Table 4) is more robust than the minimum standard deviation of depth estimates (Table 3) to define the correct SI when a nonlinear background exists. The mini-

mum standard deviation of depth estimates does not give the correct SI for all sources; it fails for the monopole and dipole cases. In addition, the nonlinear background does not need to be previously removed to perform the Euler deconvolution when base-level estimates are used to define the correct SI.

Test 3 — Strongly interfering anomalies with constant and nonlinear background

Here, we moved the position of the single pole to $x_o = 25$ km and $y_o = 38$ km and the dipole to $x_o = 20$ km and $y_o = 38$ km to give rise strongly interfering anomalies; the other sources were kept at the same position. Also, we added a polynomial nonlinear background (Figure 3b) using equation 7 to the original data (not shown) and a constant background of 47,500 nT (as in the first test shown in Figure 1). Figure 6 shows the simulated interfering magnetic data, in which we note how hard is to distinguish and locate correctly the pole-like and the dipole-like sources.

Figure 7a–7d shows the depth estimates from Euler deconvolution assuming SIs of 0, 1, 2, and 3, respectively. Like the previous test, plateaus on depth estimates are not clearly defined for the single pole (Figure 7c) and dipole (Figure 7d). The poorly disclosed plateaus in Figure 7c and 7d exhibit a smoothing oscillation being bounded by abrupt variations of the depth estimates. These results differ from the plateaus shown in Figure 2c (single pole) and 2d (dipole) in the case of synthetic test simulating weakly interfering anomalies (Figure 1). Again, this third test shows that the depth estimates are influenced by interfering anomalies, generated either by close sources or by nonlinear background. As in the previous test, we use the intersection of mapped plateaus on horizontal estimates (not shown) to delineate the areas to compute the standard deviations. Figure 7a–7d outlines these areas by the dashed rectangles.

Here, the minima standard deviations of depth estimates (Table 5) of the prism and the line of poles are able to correctly determine the SIs equal to zero and one. However, the minima standard deviations of depth estimates (Table 5) of the single pole and the dipole indicate a wrong SI = 1 because the true ones are SI = 2 (in the case of a pole-like source) and SI = 3 (in the case of a dipole-like source).

Figure 7e–7h shows the base-level estimates from Euler deconvolution by assuming SIs of 0, 1, 2, and 3, respectively. As in the previous test, the locations of the pole- and dipole-like sources are not clearly defined through the base-level estimates. Table 6 confirms that the minima standard deviations of base-level estimates are able to correctly determine the SIs, even if the anomalies strongly interfere (Figure 6). Although the minima

SI in Euler deconvolution

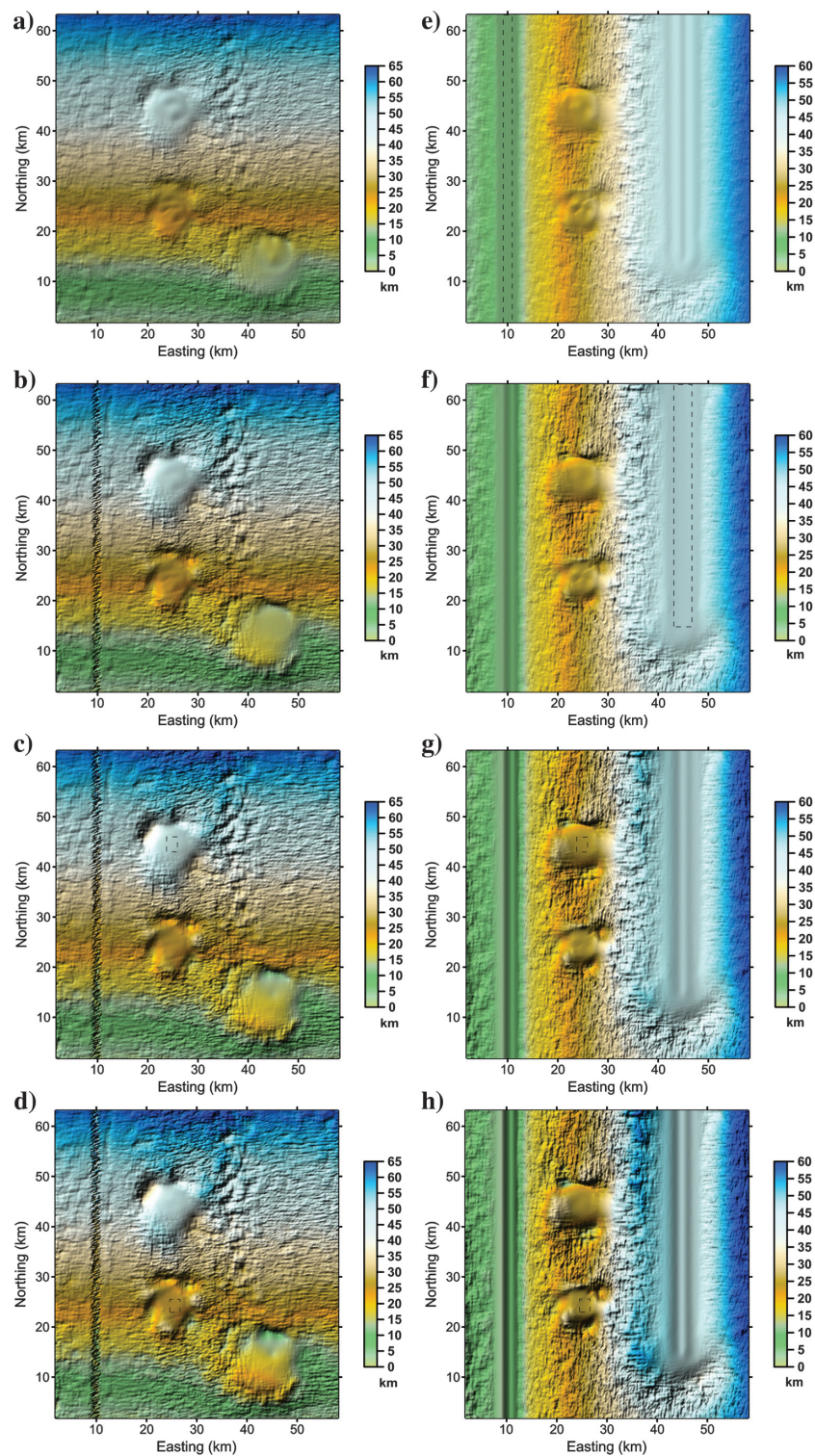


Figure 5. Euler deconvolution horizontal estimates for anomaly with nonlinear background (Figure 3c). (a-d) \hat{x}_o and (e-h) \hat{y}_o estimates assuming SIs of 0, 1, 2, and 3, respectively, for both set of estimates. For each source, the plateau areas, where the methodology is applied, are outlined by the dashed rectangles. These areas were defined by the intersection of mapped plateaus on the horizontal estimates (\hat{x}_o and \hat{y}_o).

standard deviations of base-level estimates indicate the correct sources (marked in boldface in Table 6), the differences in the standard deviations for different SIs are quite small. This happens because Euler deconvolution is applied to strongly interfering anomalies (Figure 6). Contrary to the results shown in Table 2, in which the minima standard deviations are very distinguishable because the Euler deconvolution is applied to weak-interfering anomalies (Figure 1).

In this test, we also show that base-level estimates are more robust than depth estimates to define the correct SI when strong-interfering anomalies are generated either by nearby sources or by a nonlinear background. The smallest scattering of depth estimates failed in determining the correct SI (e.g., pole and dipole cases, see Table 5). Finally, we stress that there is no theoretical restriction in applying the Euler deconvolution to total-field measurements without removing either any constant or nonlinear backgrounds.

APPLICATION TO REAL DATA SET

The GAP is a region in the central part of Brazil subject to mafic-alkaline magmatism (Marangoni and Mantovani, 2013). The region is characterized by mafic-ultramafic alkaline complexes (plutonic intrusions) in the northern portion, and subvolcanic alkaline intrusions (diatremes) in the central part and volcanic products (kamafugite lava flows) in the south with several dikes throughout the area (Junqueira-Brod et al., 2005; Dutra and Marangoni, 2009; Dutra et al., 2012). Thirteen anomalies are notable in the total-field magnetic map of GAP (Dutra et al., 2012; Marangoni and Mantovani, 2013), and these intrusions have remanent magnetization (Dutra et al., 2014; Marangoni et al., 2016).

The real aeromagnetic data were acquired between June and November 2004 with financial support from the government of the state of Goiás, Brazil (LASA Prospection and Engineer, 2004). The flight lines in the north-south direction were acquired every 500 m,

Table 3. Standard deviations of depth estimates for the nonlinear background.

Source	SI = 0	SI = 1	SI = 2	SI = 3
Prism	0.003	0.232	0.468	0.703
Line of poles	0.109	0.047	0.113	0.223
Pole	0.099	0.078	0.098	0.143
Dipole	0.120	0.092	0.081	0.099

Minimum standard deviation for each source is highlighted in boldface.

Table 4. Standard deviations of base-level estimates for the nonlinear background.

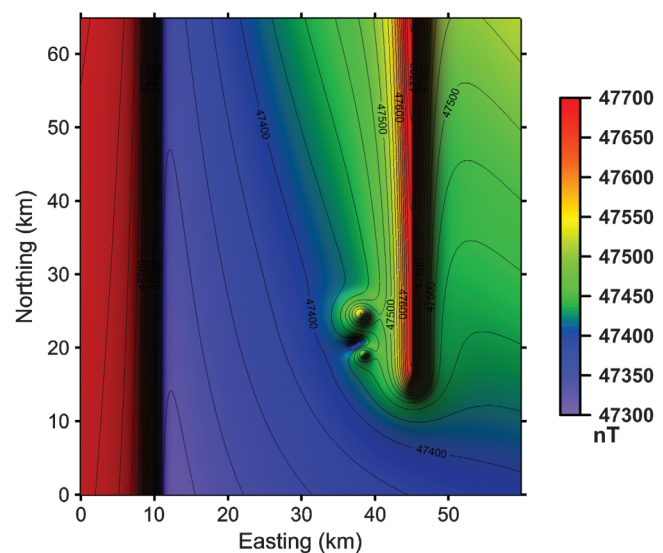
Source	SI = 0	SI = 1	SI = 2	SI = 3
Prism	98.227	115.501	116.438	116.752
Line of poles	3129.689	21.849	27.660	31.178
Pole	1862.679	11.252	5.748	6.383
Dipole	2161.655	15.889	5.532	2.974

Minimum standard deviation for each source is highlighted in boldface.

and the tie lines in the east–west direction were acquired every 5 km. The flight height was approximately constant at 100 m, and the interval between the measurements was 0.1 s, this interval resulted in one measurement at each approximately 8.2 m. The data set is gridded with the same size in the x - and y -directions, 125 m, as originally done by the data-acquisition company (LASA, 2004). Figure 8a shows the total-field anomaly in the northern portion of the GAP (Junqueira-Brod et al., 2002), and the inset shows the location of the GAP. In Figure 8a, the numbers indicate the main alkaline intrusions in this region: (1) Montes Claros de Goiás complex, (2) Diorama, (3) Córrego dos Bois complex, (4) Fazenda Buriti complex, and (5) Arenópolis.

Junqueira-Brod et al. (2002) present a detailed geologic study of this area. According to these authors, the Montes Claros de Goiás complex is an outcrop with 28 km^2 of superficial area formed by dunes, peridotites, pyroxenites, gabbros, and syenites. The ultramafic rocks form two nuclei that rise to the southwest and north, separated by a central syenitic intrusion. The Arenópolis intrusion is an elongated body generated by three distinct lithologic types: pyroxenite, melteigites, and syenite, the latter outcrops. The Córrego dos Bois complex consists of two domes, mainly of dunites, covering an area of 33 km^2 . The structure is surrounded by a narrow and discontinuous intrusion of syenite and being intruded by dikes. The Fazenda Buriti complex covers an area of 35 km^2 and consists of olivine clinopyroxenite, melagabbro, syenogabbro, and syenite (Dutra et al., 2012). Finally, in the Diorama area are common subvolcanic intrusions, dikes, plugs, and sills of picrite (Marangoni et al., 2016).

Here, we apply Euler deconvolution to the whole area, but we focus our interpretation on the magnetic anomaly over the Diorama alkaline intrusion (Dutra et al., 2014; Oliveira et al., 2015; Maran-



goni et al., 2016). The Diorama is our target anomaly because its shape resembles a weakly interfering anomalies produced by isolated sources. However, we interpret the main alkaline intrusions that yield the strongest magnetic anomalies (labeled 1–5 in Figure 8a) in our study area. Although, we interpret the strongest magnetic anomalies, we stress that there are many other weak anomalies that can generate interferences. We run Euler deconvolution with a moving data window size of 9×9 grid points. Figure 8b shows depth estimates, and Figure 8c shows base-level estimates of Euler deconvolution for the whole area assuming SI = 2. The estimates assuming other indices are not shown because there are no large plateaus as for SIs 0 and 1 and the shapes for SIs 2 and 3 are similar. Figure 8b shows many forms that seem plateaus on depth estimates. The selected plateau areas are indicated by the first letter of the name of the anomalies and delineated by the rectangles in Figure 8b. Notice that over the Diorama anomaly, we identified three plateaus (D1–D3 in Figure 8b), we could also identify these plateaus using Euler deconvolution with a window size of 15 x 15 points (not shown). On the other hand, we could not clearly identify any plateau over the anomaly Fazenda Buriti (labeled 4 in Figure 8). Base-level estimates in Figure 8c follow the same pattern of the anomalies shown in Figure 8a and exhibit nonlinear patterns of the strong and the weak anomalies. Besides, a possible poor definition of IGRF in South America can also contribute to this nonlinear pattern (Marangoni et al., 2016).

We applied our methodology and calculated the standard deviations of depth and base-level estimates assuming SIs of 0, 1, 2, and 3. Table 7 shows the minima standard deviations of base-level estimates highlighted in boldface. Based on this analysis, we may infer that the alkaline intrusion of Diorama is generated by three plug intrusions (D1–D3 in Figure 8b). Also, the results point out that Arenópolis (A1) and Montes Claros de Goiás (CM1) are dipole-like sources, and Córrego dos Bois (C1) is generated by line of poles. The unrealistic result about Córrego dos Bois complex (labeled 3 in Figure 8a) is expected because this anomaly does not seem to be produced by an ideal single-point source and thus the Euler's solutions are not reliable. In fact, it seems that it is generated by a complex source or multiple sources (a nonideal source). Let us recall that Euler deconvolution is grounded on the Euler theorem equation for homogeneous functions; hence, it should only be applied to limited situations in which it can be expected to work and under the premises previously discussed. As pointed out by Barbosa and Silva (2011), there is still more to be done to improve

Euler deconvolution to reduce its disadvantages (e.g., its poor performance in interpreting anomalies produced by nonideal sources) but without losing its advantage (e.g., computational efficiency).

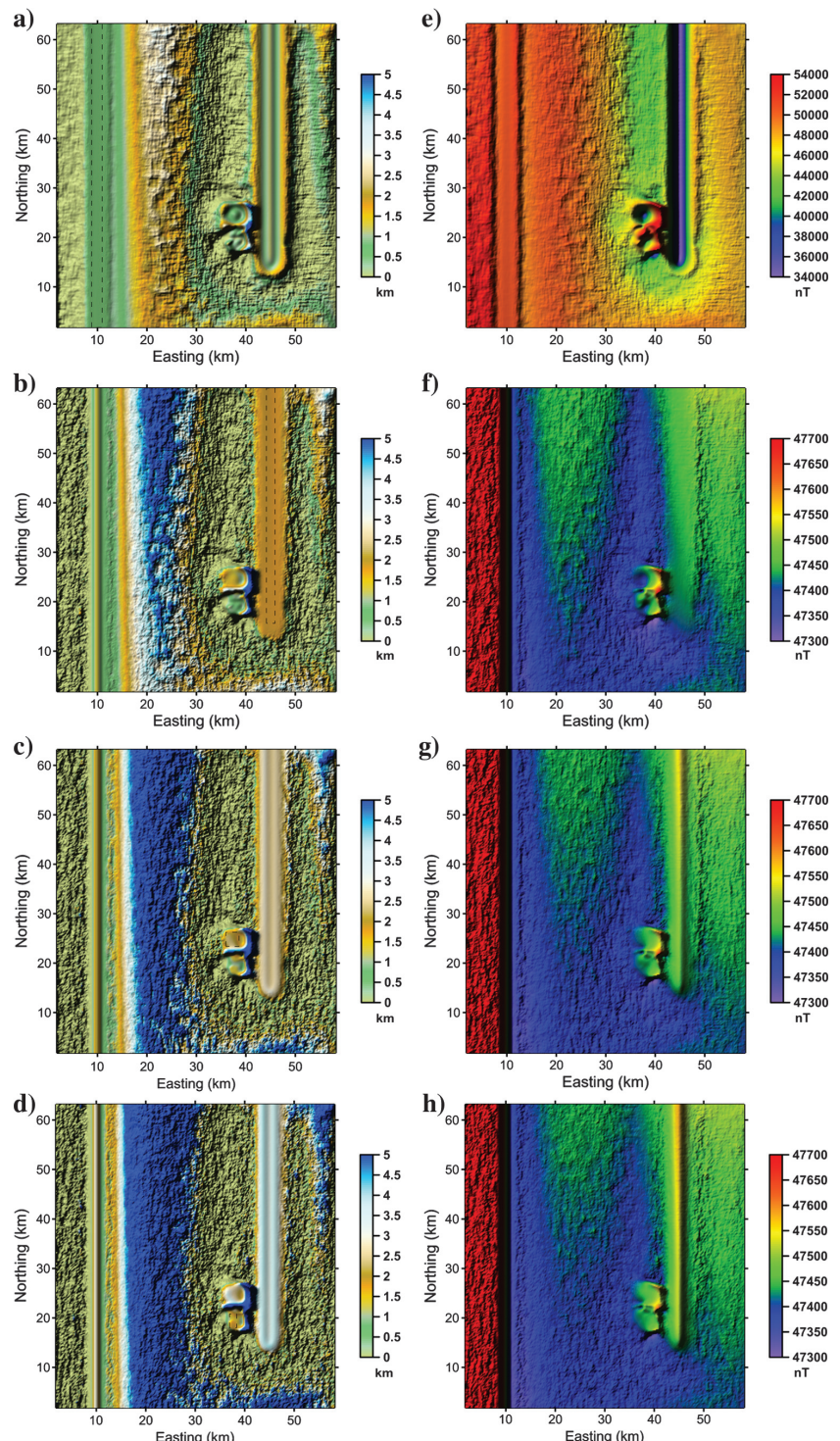


Figure 7. Euler deconvolution estimates for strong-interfering anomalies with constant and nonlinear background (Figure 6). (a-d) Depth and (e-h) base-level estimates assuming SIs of 0, 1, 2, and 3, respectively. For each source, the plateau areas, where the methodology is applied, are outlined by the dashed rectangles. These areas were defined by the intersection of mapped plateaus on horizontal estimates (\hat{x}_o and \hat{y}_o , not shown).

The most striking feature of Table 7 is the small differences in the standard deviations for different SIs. Like the synthetic test using strongly interfering anomalies (Figure 6; Table 6), in the real data set (e.g., the Diorama anomaly in Figure 8a) the differences in the standard deviations for different SIs are small (Table 7). Likewise, the real data (Figure 8a) exhibit strongly interfering anomalies. We also applied our methodology to the magnetic anomaly in which the IGRF was removed (not shown), and the results are basically the same.

Table 5. Standard deviations of depth estimates for interfering anomalies with constant and nonlinear background.

Source	SI = 0	SI = 1	SI = 2	SI = 3
Prism	0.003	0.291	0.587	0.883
Line of poles	0.100	0.038	0.115	0.213
Pole	0.169	0.136	0.188	0.301
Dipole	0.149	0.134	0.155	0.201

Minimum standard deviation for each source is highlighted in boldface.

Table 6. Standard deviations of base-level estimates for interfering anomalies with constant and nonlinear background.

Source	SI = 0	SI = 1	SI = 2	SI = 3
Prism	56.307	77.423	77.994	78.188
Line of poles	1534.905	18.558	20.280	21.493
Pole	2477.599	15.632	13.560	15.741
Dipole	3076.670	24.874	11.760	9.126

Minimum standard deviation for each source is highlighted in boldface.

Table 7. Standard deviations of base-level estimates for application to the real data set.

Source	SI = 0	SI = 1	SI = 2	SI = 3
D1	5704.204	32.492	19.851	23.163
D2	36572.570	393.546	367.408	377.060
D3	17892.637	156.249	151.961	162.679
C1	49128.473	735.896	893.910	959.535
A1	61534.789	462.392	237.158	215.245
CM1	45298.429	777.376	665.279	646.095

Minimum standard deviation for each source is highlighted in boldface. The sources are pinpointed in Figure 8b.

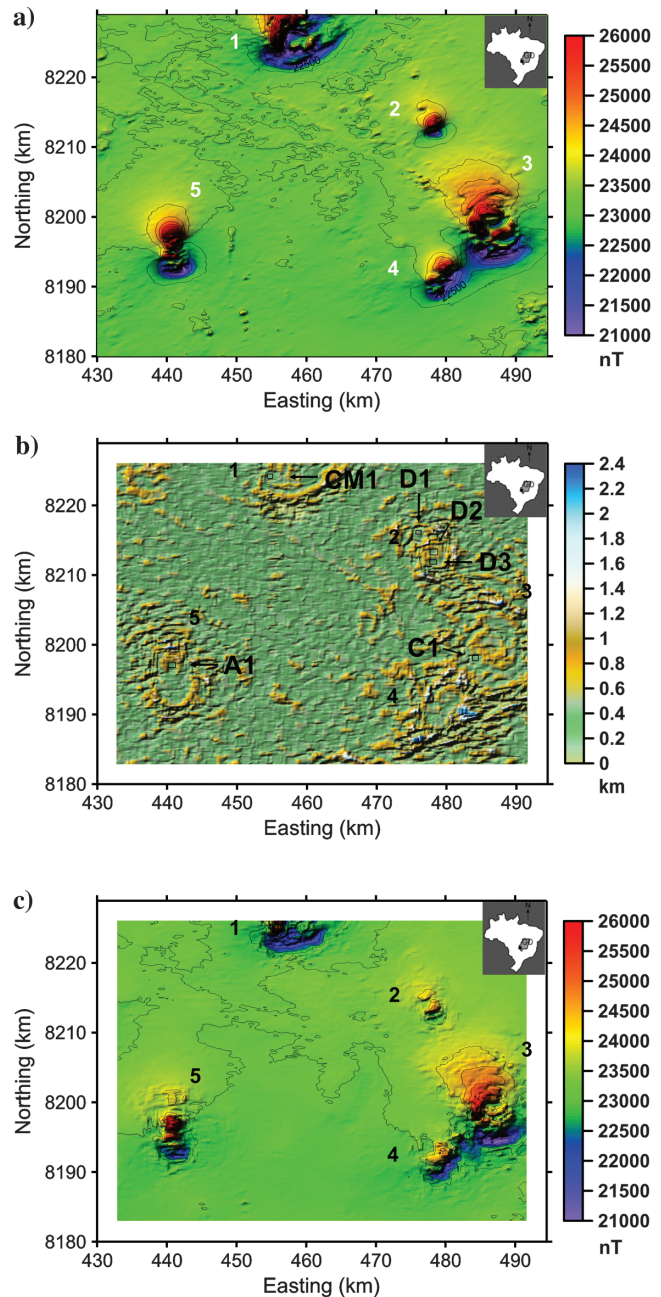


Figure 8. Real data set application. (a) Total-field anomaly in the northern portion of GAP. The numbers indicate the main alkaline intrusions in this study area: 1, Montes Claros de Goiás complex; 2, Diorama; 3, Córrego dos Bois complex; 4, Fazenda Buriti complex; and 5, Arenópolis. The inset shows the location of GAP. (b) Depth estimates assuming SI = 2. The plateau areas, where the methodology is applied, are outlined in the rectangles with the first letters of the anomalies shown in (a). (c) Base-level estimates assuming SI = 2, notice the nonlinear pattern of the base-level estimates and how they mimic the anomaly shown in (a).

CONCLUSION

By analyzing Euler's equation, we show that realizations of random variables contaminating the potential-field measurements and its gradients affect the base-level estimates if, and only if, the SI is

not assumed correctly. We proposed a methodology to define the correct SI based on the minimum standard deviation of base-level estimates. For each tentative SI, we calculate the standard deviation of base-level estimates over the geologic source which, in turn, is defined by the areas depicted as plateau-shaped depth estimates or plateau-shaped horizontal estimates. We tested our methodology with different sources, related to different the SIs and achieved the correct SI even in the case of strongly interfering anomalies. We also show that Euler deconvolution does not require that the observed total field be corrected either from constant or nonlinear backgrounds, such as IGRF or regional tendency. Actually, the presence of backgrounds and nearby sources affects depth estimates, but they do not affect base-level estimates. Consequently, the determination of the correct SI based on any criterion grounded on the depth estimates can fail. Rather, the proposed criterion for determining the correct SI based on the minimum standard deviation of base-level estimates is sound. Application to a real data set followed the expected theoretical behavior, and we infer that the alkaline intrusion over Diorama (Goiás, Brazil) is generated by three plugs, based on $SI = 2$ defined from our methodology. We applied our methodology in total-field measurements and total-field anomaly (corrected for IGRF), and the numerical results are basically the same. Both results indicate the same SI for the Diorama alkaline intrusion and show that the magnetic data do not need to be corrected for IGRF previously to the application of Euler deconvolution. Applications in areas where the anomalies do not even resemble to be generated by a single-point source (ideal source) have impracticable and unpredictable results. The standard Euler deconvolution is grounded on Euler theorem equation for homogeneous functions; hence, theoretically, it should only be applied to geologic situations in which it can be expected to work and under the premises it was developed for working. However, complex geologic scenarios should not be ignored; ergo, there is still room for improvement to modify and adapt Euler deconvolution equation to nonideal sources.

ACKNOWLEDGMENTS

The authors are particularly grateful to the assistant editor J. Shragge, the associate editor G. Florio, the reviewers R. Pasteka, A. Reid and anonymous reviewers for their questions and suggestions. F. F. Melo was supported in this research by Ph.D. scholarships from the Brazilian research agencies: CAPES and FAPERJ (grant no. E-26/200.532/2018), Brazil. V. C. F. Barbosa was supported by fellowships from the Brazilian research agencies: CNPQ (grant no. 307135/2014-4) and FAPERJ (grant no. E-26/203.091/2016). The authors would also like to thank the government of the state of Goiás, Brazil, for permission to use the real aeromagnetic data.

DATA AND MATERIALS AVAILABILITY

Data associated with this research are confidential and cannot be released.

REFERENCES

- Barbosa, V. C. F., and J. B. C. Silva, 2011, Reconstruction of geologic bodies in depth associated with a sedimentary basin using gravity and magnetic data: *Geophysical Prospecting*, **59**, 1021–1034, doi: [10.1111/j.1365-2478.2011.00997.x](https://doi.org/10.1111/j.1365-2478.2011.00997.x).
- Barbosa, V. C. F., J. B. C. Silva, and W. E. Medeiros, 1999, Stability analysis and improvement of structural index estimation in Euler deconvolution: *Geophysics*, **64**, 48–60, doi: [10.1190/1.1444529](https://doi.org/10.1190/1.1444529).
- Blakely, R. J., 1996, *Potential theory in gravity and magnetic applications*: Cambridge University Press.
- Chulliat, A., S. Macmillan, P. Alken, C. Beggan, M. Nair, B. Hamilton, A. Woods, V. Ridley, S. Maus, and A. Thomson, 2014, The US/UK World Magnetic Model for 2015–2020: NOAA National Geophysical Data Center, doi: [10.7289/V5TH8JNW](https://doi.org/10.7289/V5TH8JNW).
- Dewangan, P., T. Ramprasad, M. V. Ramana, M. Desa, and B. Shailaja, 2007, Automatic interpretation of magnetic data using Euler deconvolution with nonlinear background: *Pure and Applied Geophysics*, **164**, 2359–2372, doi: [10.1007/s00024-007-0264-x](https://doi.org/10.1007/s00024-007-0264-x).
- Dutra, A. C., and Y. R. Marangoni, 2009, Gravity and magnetic 3D inversion of Morro do Engenho complex, Central Brazil: *Journal of South American Earth Sciences*, **28**, 193–203, doi: [10.1016/j.jsames.2009.02.006](https://doi.org/10.1016/j.jsames.2009.02.006).
- Dutra, A. C., Y. R. Marangoni, and T. C. Junqueira-Brod, 2012, Investigation of the Goiás Alkaline Province, Central Brazil: Application of gravity and magnetic methods: *Journal of South American Earth Sciences*, **33**, 43–55, doi: [10.1016/j.jsames.2011.06.004](https://doi.org/10.1016/j.jsames.2011.06.004).
- Dutra, A. C., Y. R. Marangoni, and R. I. F. Trindade, 2014, Aeromagnetic and physical-chemical properties of some complexes from Goiás Alkaline Province: *Brazilian Journal of Geology*, **44**, 361–373, doi: [10.5327/Z2317-4889](https://doi.org/10.5327/Z2317-4889).
- Fairhead, J. D., K. J. Bennett, D. R. H. Gordon, and D. Huang, 1994, Euler: Beyond the “Black Box”: 64th Annual International Meeting, SEG, Expanded Abstracts, 422–424, doi: [10.1190/1.1932113](https://doi.org/10.1190/1.1932113).
- Fedi, M., G. Florio, and V. Paoletti, 2015, MHODE: A local-homogeneity theory for improved source-parameter estimation of potential fields: *Geophysical Journal International*, **202**, 887–900, doi: [10.1093/gji/ggv185](https://doi.org/10.1093/gji/ggv185).
- Fedi, M., G. Florio, and T. A. M. Quarta, 2009, Multiridge analysis of potential fields: Geometric method and reduced Euler deconvolution: *Geophysics*, **74**, no. 4, L53–L65, doi: [10.1190/1.3142722](https://doi.org/10.1190/1.3142722).
- Florio, G., and M. Fedi, 2014, Multiridge Euler deconvolution: *Geophysical Prospecting*, **62**, 333–351, doi: [10.1111/1365-2478.12078](https://doi.org/10.1111/1365-2478.12078).
- Gerovska, D., and M. J. Araújo-Bravo, 2003, Automatic interpretation of magnetic data based on Euler deconvolution with unprescribed structural index: *Computers and Geosciences*, **29**, 949–960, doi: [10.1016/S0098-3004\(03\)00101-8](https://doi.org/10.1016/S0098-3004(03)00101-8).
- Henderson, R. G., and I. Zietz, 1948, Analysis of total magnetic-intensity anomalies produced by point and line sources: *Geophysics*, **13**, 428–436, doi: [10.1190/1.1437414](https://doi.org/10.1190/1.1437414).
- Hinze, W. J., R. R. Von Frese, and A. H. Saad, 2013, *Gravity and magnetic exploration: Principles, practices, and applications*: Cambridge University Press.
- Hood, P., 1965, Gradient measurements in aeromagnetic surveying: *Geophysics*, **30**, 891–902, doi: [10.1190/1.1439666](https://doi.org/10.1190/1.1439666).
- Hsu, S., 2002, Imaging magnetic sources using Euler’s equation: *Geophysical Prospecting*, **50**, 15–25, doi: [10.1046/j.1365-2478.2001.00282.x](https://doi.org/10.1046/j.1365-2478.2001.00282.x).
- Junqueira-Brod, T. C., J. C. Gaspar, J. A. Brod, H. Jost, E. S. R. Barbosa, and C. V. Kafino, 2005, Emplacement of kamafugite lavas from the Goiás Alkaline Province, Brazil: Constraints from whole-rock simulations: *Journal of South American Earth Sciences*, **18**, 323–335, doi: [10.1016/j.jsames.2004.11.001](https://doi.org/10.1016/j.jsames.2004.11.001).
- Junqueira-Brod, T. C., H. L. Roig, J. C. Gaspar, J. A. Brod, and P. R. Meneses, 2002, A Província Alcalina de Goiás e a extensão de seu vulcanismo kamafugítico: *Revista Brasileira de Geociências*, **32**, 559–566, doi: [10.25249/0375-7536.2002324559566](https://doi.org/10.25249/0375-7536.2002324559566).
- Keating, P., and M. Pilkington, 2004, Euler deconvolution of the analytic signal and its application to magnetic interpretation: *Geophysical Prospecting*, **52**, 165–182, doi: [10.1111/j.1365-2478.2004.00408.x](https://doi.org/10.1111/j.1365-2478.2004.00408.x).
- LASA Prospection and Engineer S.A., 2004, Project: Aerogeophysical survey of Goiás state, first phase: Survey and data processing: Final report, Rio de Janeiro, SGM/MME/CPRM and SIC/SGM/FUNMINERAL/Goiás State, Brazil, vol. 22 and maps.
- Marangoni, Y. R., and M. S. M. Mantovani, 2013, Geophysical signatures of the alkaline intrusions bordering the Paraná Basin: *Journal of South American Earth Sciences*, **41**, 83–98, doi: [10.1016/j.jsames.2012.08.004](https://doi.org/10.1016/j.jsames.2012.08.004).
- Marangoni, Y. R., H. Zhang, and H. J. Ferreira, 2016, Gravity and magnetic integrated data interpretation of the Córrego dos Bois complex, Goiás Alkaline Province, central Brazil: *Revista Brasileira de Geofísica*, **33**, 599–610.
- Mas-Colell, A., M. D. Whinston, and J. R. Green, 1995, *Microeconomic theory*: Oxford University Press.
- Melo, F. F., V. C. F. Barbosa, L. Uieda, V. C. Oliveira, Jr., and J. B. C. Silva, 2013, Estimating the nature and the horizontal and vertical positions of 3D magnetic sources using Euler deconvolution: *Geophysics*, **78**, no. 6, J87–J98, doi: [10.1190/geo2012-0515.1](https://doi.org/10.1190/geo2012-0515.1).
- Mikhailov, V., A. Galdeano, M. Diament, A. Gvishiani, S. Agayan, S. Bogoutdinov, E. Graeva, and P. Sailhac, 2003, Application of artificial intelligence for Euler solutions clustering: *Geophysics*, **68**, 168–180, doi: [10.1190/1.1543204](https://doi.org/10.1190/1.1543204).
- Mushayandebvu, M. F., P. van Driel, A. B. Reid, and J. D. Fairhead, 2001, Magnetic source parameters of two-dimensional structures using extended Euler deconvolution: *Geophysics*, **66**, 814–823, doi: [10.1190/1.1444971](https://doi.org/10.1190/1.1444971).

- Nabighian, M. N., and R. O. Hansen, 2001, Unification of Euler and Werner deconvolution in three dimensions via the generalized Hilbert transform: *Geophysics*, **66**, 1805–1810, doi: [10.1190/1.1487122](https://doi.org/10.1190/1.1487122).
- Oliveira, V. C., Jr., D. P. Sales, V. C. F. Barbosa, and L. Uieda, 2015, Estimation of the total magnetization direction of approximately spherical bodies: *Nonlinear Processes in Geophysics*, **22**, 215–232, doi: [10.5194/npg-22-215-2015](https://doi.org/10.5194/npg-22-215-2015).
- Pasteka, R., 2006, The role of the interference polynomial in the Euler deconvolution algorithm: *Bollettino di Geofisica Teorica ed Applicata*, **47**, 171–180.
- Ravat, D., 1996, Analysis of the Euler method and its applicability in environmental magnetic investigations: *Journal of Environmental and Engineering Geophysics*, **1**, 229–238, doi: [10.4133/JEEG1.3.229](https://doi.org/10.4133/JEEG1.3.229).
- Reid, A. B., J. M. Allsop, H. Granser, A. J. Millett, and I. W. Somerton, 1990, Magnetic interpretation in three dimensions using Euler deconvolution: *Geophysics*, **55**, 80–91, doi: [10.1190/1.1442774](https://doi.org/10.1190/1.1442774).
- Reid, A. B., J. Ebbing, and S. J. Webb, 2014, Avoidable Euler errors — The use and abuse of Euler deconvolution applied to potential fields: *Geophysical Prospecting*, **62**, 1162–1168, doi: [10.1111/1365-2478.12119](https://doi.org/10.1111/1365-2478.12119).
- Reid, A. B., and J. B. Thurston, 2014, The structural index in gravity and magnetic interpretation: Errors, uses, and abuses: *Geophysics*, **79**, no. 4, J61–J66, doi: [10.1190/geo2013-0235.1](https://doi.org/10.1190/geo2013-0235.1).
- Silva, J. B. C., and V. C. F. Barbosa, 2003, 3D Euler deconvolution: Theoretical basis for automatically selecting good solutions: *Geophysics*, **68**, 1962–1968, doi: [10.1190/1.1635050](https://doi.org/10.1190/1.1635050).
- Silva, J. B. C., V. C. F. Barbosa, and W. E. Medeiros, 2001, Scattering, symmetry, and bias analysis of source-position estimates in Euler deconvolution and its practical implications: *Geophysics*, **66**, 1149–1156, doi: [10.1190/1.1487062](https://doi.org/10.1190/1.1487062).
- Smellie, D. W., 1956, Elementary approximations in aeromagnetic interpretation: *Geophysics*, **21**, 1021–1040, doi: [10.1190/1.1438294](https://doi.org/10.1190/1.1438294).
- Stavrev, P., and A. B. Reid, 2007, Degrees of homogeneity of potential fields and structural indices of Euler deconvolution: *Geophysics*, **72**, no. 1, L1–L12, doi: [10.1190/1.2400010](https://doi.org/10.1190/1.2400010).
- Stavrev, P., and A. Reid, 2010, Euler deconvolution of gravity anomalies from thick contact/fault structures with extended negative structural index: *Geophysics*, **75**, no. 6, I51–I58, doi: [10.1190/1.3506559](https://doi.org/10.1190/1.3506559).
- Stavrev, P. Y., 1997, Euler deconvolution using differential similarity transformations of gravity or magnetic anomalies: *Geophysical Prospecting*, **45**, 207–246, doi: [10.1046/j.1365-2478.1997.00331.x](https://doi.org/10.1046/j.1365-2478.1997.00331.x).
- Thompson, D. T., 1982, EULDPH: A new technique for making computer-assisted depth estimates from magnetic data: *Geophysics*, **47**, 31–37, doi: [10.1190/1.1441278](https://doi.org/10.1190/1.1441278).
- Thurston, J., 2010, Euler deconvolution in the presence of sheets with finite widths: *Geophysics*, **75**, no. 3, L71–L78, doi: [10.1190/1.3428484](https://doi.org/10.1190/1.3428484).
- Ugalde, H., and W. A. Morris, 2010, Cluster analysis of Euler deconvolution solutions: New filtering techniques and geologic strike determination: *Geophysics*, **75**, no. 3, L61–L70, doi: [10.1190/1.3429997](https://doi.org/10.1190/1.3429997).
- Uieda, L., V. C. Oliveira, Jr., and V. C. F. Barbosa, 2014, Geophysical tutorial: Euler deconvolution of potential-field data: *The Leading Edge*, **33**, 448–450, doi: [10.1190/tle33040448.1](https://doi.org/10.1190/tle33040448.1).